

SEMICONDUCTOR STRUCTURES, LOW-DIMENSIONAL SYSTEMS,
AND QUANTUM PHENOMENA

Manganese-Doped ZnS QDs: an Investigation into the Optimal Amount of Doping

S. Tomar^{a,b}, S. Gupta^b, S. Mukherjee^c, A. Singh^d, S. Kumar^e, and R. K. Choubey^{b,*}

^a Applied Science and Humanities Department, ABES Engineering College, Campus-1, 19th KM Stone, NH-24, Ghaziabad U.P., 201009 India

^b Department of Applied Physics, Amity Institute of Applied Sciences (ALIAS), Amity University, Noida Campus, Sector-125, Noida, Uttar Pradesh, 201313 India

^c Department of Physics, National Institute of Technology, Patna, Bihar, 800005 India

^d Department of Physics, Faculty of Natural Sciences Jamia Millia Islamia, Central University, New Delhi, 110025, India

^e Department of Physics, Indira Gandhi University, Meerpur, Rewari, Haryana, 122502 India

*e-mail: ravikantchoubey@gmail.com

Received July 7, 2020; revised July 7, 2020; accepted July 15, 2020

Abstract—In the present study, undoped and Mn-doped ZnS, $Zn_{1-x}Mn_xS$ ($x = 0, 0.02, 0.06, 0.10$) quantum dots (QDs) were successfully synthesized using the simple co-precipitation method. The synthesized samples were thoroughly studied using X-ray diffraction (XRD), UV-visible absorption, high-resolution transmission electron microscopy (HRTEM) with selected area of the electron diffraction, scanning electron microscope with energy dispersive X-ray spectra, photoluminescence emission (PLE), and Fourier transform infrared spectroscopy. The XRD pattern confirmed the cubic zinc-blende phase at low doping concentration; however, at higher Mn-doping concentration hetaerolite phase formation was observed. The calculated particle size using Debye–Scherrer relation was found between 1.90–2.35 nm, which was also confirmed by HRTEM analysis. The blue shift in the absorption peak of all the prepared ZnS QDs as compared to bulk ZnS was indicative of the formation of nanoparticles and the calculated band gap was in the range of 3.94–4.11 eV. The PLE spectroscopy of the synthesized QDs was performed at the excitation wavelength of 280 nm and corresponding emission spectroscopy confirmed the surface defects in synthesized ZnS QDs.

Keywords: ZnS:Mn, quantum dots, XRD, photoluminescence emission

DOI: 10.1134/S106378262011024X

1. INTRODUCTION

II–VI semiconductor quantum dots (QDs) are very important materials because of their unique physico-chemical, optical, and electronic properties owing to the well-known quantum confinement effect [1–3]. In semiconductor QDs, the band gap increases due to the decrease in particle size; when the dimensions of nano-crystallites approach the exciton Bohr radius, a blue shift in energy is observed due to the quantum confinement phenomenon. The extremely small size of QDs renders their optical and electronic properties different from those of the corresponding bulk materials. It is well reported that Cd-based chalcogenides such as CdS, CdSe, and CdTe have been frequently used for optoelectronics and biological applications [4, 5]. Due to the toxic behavior of Cd, the applicability of the Cd-based QDs is restricted in biological applications; it also causes severe environmental problems [6, 7]. These problems have stimulated researchers to develop Cd-free chalcogenides.

In the family of II–VI semiconductors, zinc sulfide (ZnS) is an important environmentally-friendly semiconducting material. ZnS, which is an important wide band gap (3.66 eV at 300 K) material, has numerous potential applications such as UV light-emitting diodes, efficient phosphors in flat-panel displays, photovoltaic devices, infrared windows, electroluminescence, sensors, etc. [8]. But, the use of ZnS is restricted within the blue-light region of the electromagnetic spectra and hence limited its application at longer wavelengths [9]. The optical properties of the pure ZnS can be easily tuned by using suitable dopant for the desired applications in the area of optoelectronic devices [10]. Doping with transition metal ions not only enhances the optical transition efficiency and increases the number of luminescent centers but also induces them to exhibit interesting magneto-optical properties [11–13]. Recently, Zha et al. reported the blue shift in band gap in Co and Ni co-doped ZnS nanorods [14]; the shifting of Raman modes in Ce, Cu co-doped ZnS nanoparticles have been studied by Harish and coworkers [15].

In the present study, we have synthesized a series of pure and manganese-doped $\text{Zn}_{1-x}\text{Mn}_x\text{S}$ ($x = 0, 0.02, 0.06, 0.10$) QDs using co-precipitation method. The evolution of the structural, morphological, and optical properties of the all synthesized QDs have been studied by X-ray diffraction (XRD) and energy dispersive X-ray (EDX) analysis, scanning electron microscopy (SEM), high-resolution transmission electron microscopy (HRTEM), as well as UV-visible, photoluminescence emission (PLE), and Fourier transform infrared (FTIR) spectroscopy.

2. EXPERIMENTAL DETAILS

2.1. Synthesis

Pristine and manganese-doped ZnS QDs were synthesized using the simple co-precipitation method [16]. Zinc acetate dihydrate [$\text{Zn}(\text{CH}_3\text{CO}_2)_2 \cdot 2\text{H}_2\text{O}$] was used as the zinc source, thioacetamide [TAA, $\text{C}_2\text{H}_5\text{NS}$] was used as the sulphur source, manganese(II) chloride [MnCl_2] was used as the manganese source, and polyvinyl pyrrolidone [PVP, average molecular weight 40000] was used as the surfactant; reagents were obtained from Sigma-Aldrich and were used without further purification. 1 g of PVP was dissolved in 200 mL of distilled water with vigorous stirring at room temperature. Precisely measured amount of zinc source was then added to this and continued vigorous stirring was maintained for 30 min. at room temperature. Then, to make a 0.02-M solution of ZnS, measured amount of sulphur source was added, and vigorous stirring was continued for 90 min at 85°C. Then, NaOH solution was titrated very slowly into the solution with constant stirring at room temperature until a pH of 10 was achieved and complete precipitation had occurred. After letting the precipitate settle for a few minutes, the supernatant liquid was discarded, and the precipitate was distributed among test tubes to be centrifuged and washed. To make the pH neutral and remove all unreacted material, impurity, and excess water, the precipitate was washed with distilled water and ethanol. The washed precipitate was collected in a Petri dish with a little bit of ethanol and allowed to dry in ambient conditions for one day. Afterwards, the ethanol had evaporated, the dry powder left behind was lightly grinded using a mortar and pestle, then collected and weighed.

The same procedure was used to synthesize the Mn-doped ZnS QDs; a measured amount of the manganese source was added along with the zinc source according to the desired doping concentration of the sample being synthesized. All the obtained samples were in a fine powder form, and while the pristine ZnS sample exhibited a white color, the manganese doped samples exhibited increasingly brown coloration with increasing doping percentage. These powder samples were used for all characterizations.

2.2. Characterizations

Rigaku Ultima IV X-ray Diffractometer (CuK_α radiation, 1.54056 Å) operated at 40 kV and 40 mA with a scanning rate of $0.02^\circ \text{ s}^{-1}$ was used to perform powder X-ray Diffraction (P-XRD). JEOL JEM-2100F with accelerating voltage of 200 kV was used to record HRTEM images. ZEISS SIGMA VP with EDX was used to record SEM images. PerkinElmer LAMBDA 750 was used to perform UV-visible absorption spectroscopy in the range of 200–600 nm.

HORIBA Scientific FluoroMax-4 at an excitation wavelength of 280 nm was used to perform PLE spectroscopy in the range of 300–500 nm. Bruker TENSOR 37 was used to perform FTIR spectroscopy. All characterizations were carried out at room temperature.

3. RESULTS AND DISCUSSION

3.1. Structural Studies

Figure 1 shows the powder X-ray diffraction plots of the $\text{Zn}_{1-x}\text{Mn}_x\text{S}$ ($x = 0, 0.02, 0.06, 0.10$) QDs. The peaks obtained from the P-XRD pattern of the $\text{Zn}_{1-x}\text{Mn}_x\text{S}$ QDs are (111), (220), and (311), which is well matched with the Powder Diffraction File no. 05-0566 of the cubic zinc-blende phase of ZnS.

Analysis of the P-XRD pattern of the $\text{Zn}_{0.98}\text{Mn}_{0.02}\text{S}$ QD sample indicates that the relatively lower doping concentration (2%) of manganese into the ZnS QD lattice has not caused a secondary phase to occur, implying that the relatively small amount of manganese ions have occupied the substitutional zinc and/or interstitial sites in the ZnS QD lattice without drastically changing the structure of the unit cell of the cubic zinc-blende phase of ZnS. Analysis of the P-XRD pattern of the $\text{Zn}_{0.94}\text{Mn}_{0.06}\text{S}$ and $\text{Zn}_{0.90}\text{Mn}_{0.10}\text{S}$ QD samples indicates that at a relatively higher doping concentration (6 and 10%) of manganese in the ZnS QD lattice, a secondary phase was formed, implying that the manganese ions have not only occupied the substitutional zinc and/or interstitial sites in the ZnS QD lattice, but have also, at higher concentrations, formed a new compound that has a different unit cell structure than that of the unit cell of the cubic zinc-blende phase of ZnS. The impurity phase was found to be the hetaerolite phase, which is ZnMn_2O_4 and the peaks corresponding to it are marked as “H” in Fig. 1.

The P-XRD peaks of the $\text{Zn}_{1-x}\text{Mn}_x\text{S}$ QDs show considerable broadening, which indicates the strong confinement of the quantum dots. The highest intensity (111) peak of the P-XRD pattern of the $\text{Zn}_{1-x}\text{Mn}_x\text{S}$ ($x = 0, 0.02, 0.06, 0.10$) QDs centered at a mean 29.15° has been Gauss fitted to calculate the lower limit of the average crystallite size D of the quan-

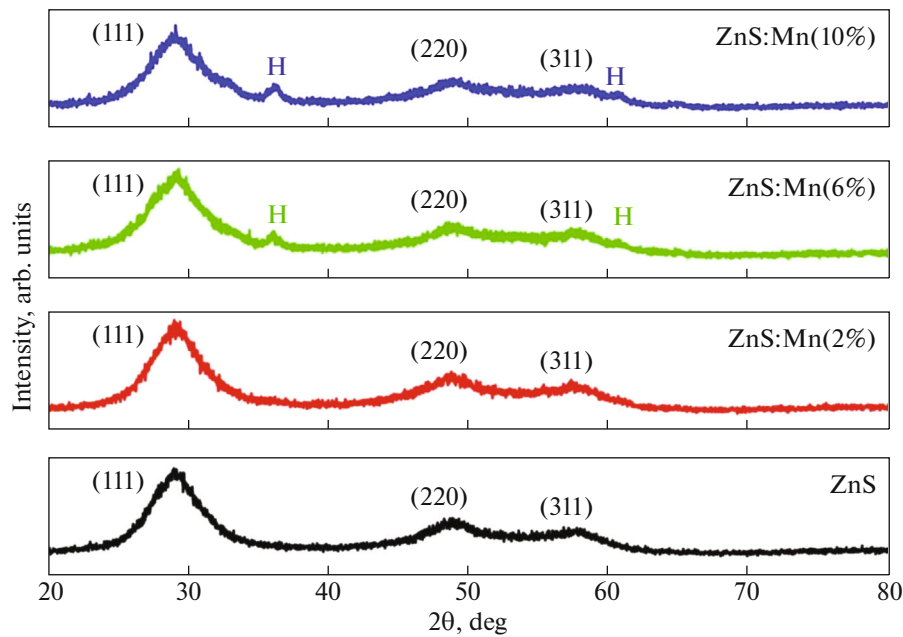


Fig. 1. P-XRD plots of the $Zn_{1-x}Mn_xS$ ($x = 0, 0.02, 0.06, 0.10$) QDs.

tum dots using the Debye-Scherrer formula [18, 19], which is

$$D = \frac{k\lambda}{\beta \cos \theta} \frac{180}{\pi}, \quad (1)$$

where λ is the wavelength of the incident X-ray beam ($= 0.154056$ nm for CuK_{α} radiation), k is the sphericity factor ($= 0.9$ for spherical particles), and β , θ are the full-width half-maximum and Bragg's diffraction angle, respectively, of the highest intensity (111) characteristic peak. Lattice parameter a of the unit cell of the cubic zinc-blende phase of the $Zn_{1-x}Mn_xS$ ($x = 0, 0.02, 0.06, 0.10$) QDs was calculated using the formula,

$$\alpha = d_{hkl} \sqrt{h^2 + k^2 + l^2} = \frac{\lambda}{2 \sin \theta} \sqrt{h^2 + k^2 + l^2}, \quad (2)$$

where h, k, l are the Miller indices of the (111) lattice plane and d_{hkl} is the interplanar spacing between two consecutive (111) lattice planes.

The Bohr excitonic radius for a substance is the limiting radius of the exciton (bound electron-hole pair), or the limiting size of a particle; the material will exhibit strong quantum confinement effects if its size is smaller than its Bohr excitonic radius. The Bohr excitonic radius of ZnS is approximately 2.6 nm [16]. Table 1 shows the comparison of the lower limit of average crystallite sizes and lattice parameters of the cubic zinc-blende phase of the $Zn_{1-x}Mn_xS$ ($x = 0, 0.02, 0.06, 0.10$) QDs.

From Debye-Scherrer calculations, it can be observed that manganese-doped ZnS QDs have average crystallite size smaller than the Bohr excitonic radius.

3.2. UV-Visible Absorption Spectroscopy

Figure 2 shows the UV-visible absorption plot of the $Zn_{1-x}Mn_xS$ ($x = 0, 0.02, 0.06, 0.10$) QDs. The undoped ZnS QDs show absorption peak at ~ 310 nm while for $Zn_{1-x}Mn_xS$ ($x = 0.02, 0.06, 0.10$) QDs

Table 1. Comparison of the structural and optical parameters of the $Zn_{1-x}Mn_xS$ ($x = 0, 0.02, 0.06, 0.10$) QDs

SAMPLE	Average crystallite size (Debye-Scherrer formula), nm	Lattice parameter a , Å	Band gap (Tauc plot), eV	Particle size (Brus equation), nm	Absorption edge λ_a , nm	Blue shift w.r.t. bulk ZnS, nm	Blue shift w.r.t. pristine ZnS QD, nm
ZnS (pristine)	2.26	5.3035	3.94	2.35	314.6	22.4	—
$Zn_{0.98}Mn_{0.02}S$	2.21	5.2893	4.11	1.91	301.6	35.4	13
$Zn_{0.94}Mn_{0.06}S$	1.96	5.2297	4.15	1.84	298.7	38.3	15.9
$Zn_{0.90}Mn_{0.10}S$	2.19	5.2721	4.09	1.97	303.8	33.2	10.8

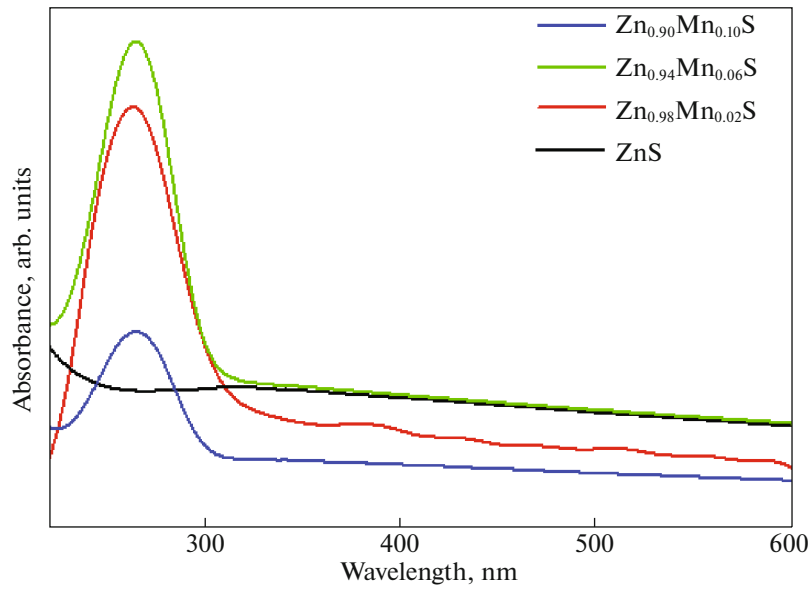


Fig. 2. UV-visible absorption plot of the $Zn_{1-x}Mn_xS$ ($x = 0, 0.02, 0.06, 0.10$) QDs.

exhibit absorption peaks at 265, 262, and 267 nm, respectively.

It can be clearly noticed that all the absorption peaks are blue-shifted as compared to bulk ZnS (340 nm), which indicates the formation of nanoparticles in all the samples. Further, blue shifting in Mn-doped ZnS QDs as compared to ZnS (pristine) QDs and corresponding reduction in particle size can be observed; the results are summarized in Table 1 above.

Energy band gap values of the $Zn_{1-x}Mn_xS$ ($x = 0, 0.02, 0.06, 0.10$) QDs were determined from the UV-visible absorption data using the Tauc relation [21], which is

$$(\alpha h\nu)^n = \beta(h\nu - E_g), \quad (3)$$

where β is an arbitrary constant, ν is the frequency of the photon ($= c/\lambda$, where λ is the wavelength of the photon and c is the speed of light in vacuum), h is the Planck constant, E_g is the energy band gap, $n = 2$ for direct band gap semiconductors (like ZnS), and α is the absorption coefficient ($= 2.303A/t$, where $t = 1$ cm is the thickness of the cuvette, and A is the absorbance at a specific wavelength). A graph is then plotted between E_g on the x -axis and $(\alpha h\nu)^2$ on the y -axis, so that the value of the energy band gap for the QD sample can be obtained by extrapolating the linear portion of the graph to the x -axis. Figure 3 shows the Tauc plots of the $Zn_{1-x}Mn_xS$ ($x = 0, 0.02, 0.06, 0.10$) QDs. The calculated values of the energy band gap obtained from the Tauc plots can be seen in Table 1.

It can be noticed that the energy band gap of the material initially increases with an increase in the dopant concentration until it reaches a saturated value in the 6% manganese-doped ZnS QD sample, after

which it decreases with a subsequent increase in dopant concentration. It can also be manifested from Fig. 3 that the calculated band gap values of all the QDs are higher than that of their bulk counterparts, due to well-known quantum confinement theory, in which the lowest energy of the optical transition from the valence to conduction band increases, and consequently, an increase in the band gap is observed. Also, we can notice that the $Zn_{0.94}Mn_{0.06}S$ QDs have maximum band gap, i.e., 4.15 eV, which shows better confinement effect compared to other doped and undoped QDs, while strong quantum confinement effect is observed in all the ZnS QDs in comparison to the bulk ZnS which has a band gap of 3.68 eV.

Absorption edge λ_a of the $Zn_{1-x}Mn_xS$ QDs was also calculated from the energy band gaps obtained from the Tauc plots using the relation

$$\lambda_a = \frac{hc}{E_g}. \quad (4)$$

Table 1 shows the absorption edge of the $Zn_{1-x}Mn_xS$ ($x = 0, 0.02, 0.06, 0.10$) QDs obtained from the above calculations. The blue shift in the absorption edges of the $Zn_{1-x}Mn_xS$ ($x = 0, 0.02, 0.06, 0.10$) QDs as compared to the bulk ZnS (~ 337 nm) can be clearly seen. Also, blue shift in absorption edge is observed due to Mn doping as compared to the pristine ZnS QDs.

Table 1 also shows the particle size of the $Zn_{1-x}Mn_xS$ ($x = 0, 0.02, 0.06, 0.10$) QDs calculated using the effective mass approximation model of Brus [22]. The Brus equation is

$$E_g^{nano} = E_g^{bulk} + \frac{\hbar^2 \pi^2}{2\mu R^2} - \frac{1.8e^2}{4\pi\epsilon_0\epsilon_r R}, \quad (5)$$

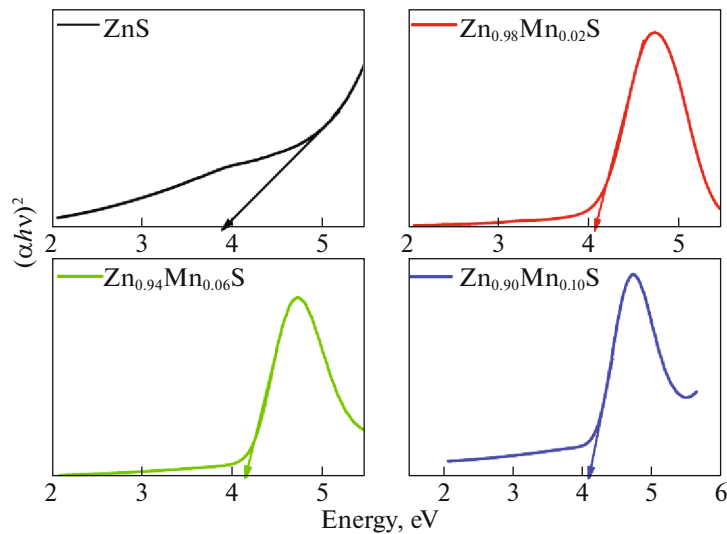


Fig. 3. Tauc plots of the $Zn_{1-x}Mn_xS$ ($x = 0, 0.02, 0.06, 0.10$) QDs.

where R is the particle size of the quantum dot, E_g^{bulk} is the energy band gap of the bulk semiconductor ($=3.68$ eV for cubic zinc-blende ZnS), E_g^{nano} is the energy band gap of the QD obtained from the Tauc plot, \hbar is the reduced Planck constant, e is the elementary charge of an electron, μ is reduced mass of the electron–hole pair [16], ϵ_0 is the permittivity of free space, and ϵ_r is the relative permittivity of ZnS ($=8.9$). The third term on the right-hand side of the Brus equation acts to decrease the energy band gap of the QD because it arises due to the Coulomb interaction between the electron–hole pair. The second term on the right-hand side of the Brus equation acts to increase the energy band gap of the QD because it arises due to the strong quantum confinement of the exciton. Brus equation calculations reveal that the particle size initially decreases with an increase of the dopant concentration, until it reaches a saturated value in the 6% manganese-doped ZnS QD sample, after which it increases with a subsequent increase of the dopant concentration. Brus equation calculations also support the findings from the structural characterizations stated in the previous section.

3.3. High-Resolution Transmission Electron Microscopy Studies

Figure 4 shows the transmission electron micrograph for the $Zn_{0.98}Mn_{0.02}S$ QD sample.

The micrograph shows that the sample has good monodispersity of spherical nanoparticles, with an average particle size of approximately 2.5 nm, which supports the evidence of strong quantum confinement shown by the P-XRD plots. The top-left inset shows selected area of the electron diffraction (SAED) pattern of $Zn_{0.98}Mn_{0.02}S$ QDs, in which the presence of

three planes can be clearly observed. The SAED pattern clearly indicates a set of uniform sharp rings, instead of spots, corresponding to diffraction from all the three planes of the nano-crystallites due to the random orientation of the crystallites. These rings represent the lattice planes (111), (220), and (311) of the cubic phase of ZnS, which is obviously in good agreement with the P-XRD pattern of $Zn_{0.98}Mn_{0.02}S$; also the most intense reflection corresponds to plane (111), which is again the confirmation of P-XRD pattern. The top-right inset shows the magnified HRTEM image of the $Zn_{0.98}Mn_{0.02}S$ QDs with the (111) lattice

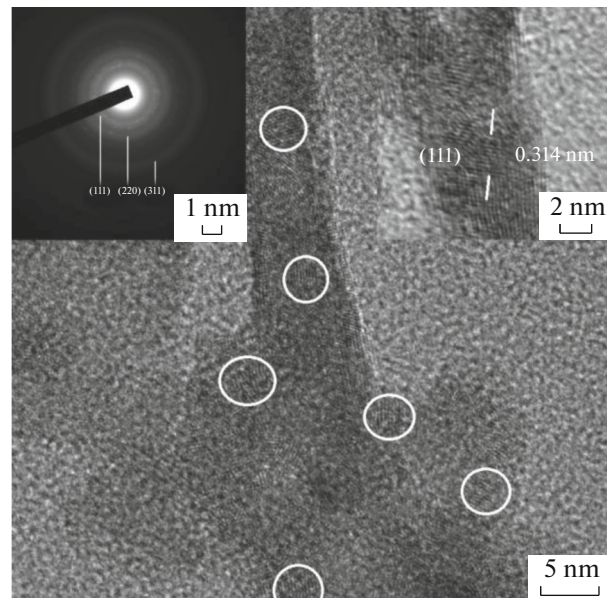


Fig. 4. Transmission electron micrograph of the $Zn_{0.98}Mn_{0.02}S$ QDs.

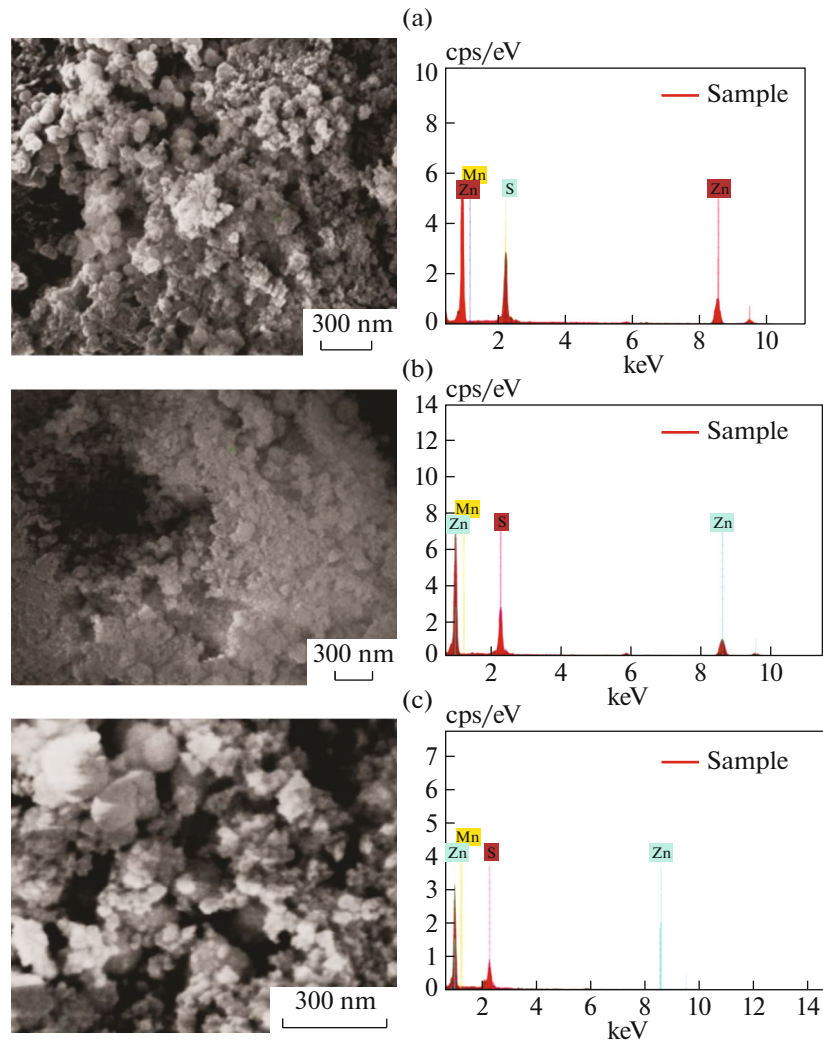


Fig. 5. SEM micrograph and EDX of the $Zn_{1-x}Mn_xS$ ($x = 0.02, 0.06, 0.10$) QDs.

planes. High crystallinity in the nanoparticles indicated by the lattice fringes in this HRTEM image is found to be 0.314 nm, which corresponds to the interplanar distance of (111) plane in cubic phase of ZnS and is very well supported by previously published reports [24, 25].

3.4. Scanning Electron Microscopy Studies

In Fig. 5, the textural features of Mn doped ZnS QDs were investigated using SEM with corresponding EDX analysis. The SEM images of these QDs are shown in Figs. 5a–5c, representing change in morphology due to increase in Mn concentration in ZnS QDs.

SEM micrograph of $Zn_{0.98}Mn_{0.02}S$ depicted in Fig. 5a has non-uniform distribution of spherical particles and they consist of single particles; however, due to further increase in Mn concentration ($Zn_{0.94}Mn_{0.06}S$ and $Zn_{0.90}Mn_{0.10}S$, Figs. 5b and 5c on

the left, respectively) cluster formation can be observed. The elemental composition determined through EDX attached with SEM instrument is also shown in Figs. 5a–5c on the right, for $Zn_{1-x}Mn_xS$ ($x = 0.02, 0.06, 0.10$) QDs, respectively. The incorporation of Mn^{2+} ions into ZnS lattice sites can be clearly revealed from EDX analysis.

3.5. Photoluminescent Emission Spectroscopy

Figure 6 shows the PLE plot of the $Zn_{1-x}Mn_xS$ ($x = 0, 0.02, 0.06, 0.10$) QDs.

Surface defects occur in the QD samples because of the large surface-to-volume ratio caused by very small size of QDs as supported by the structural characterizations and the Brus equation calculations. Formation of excitons due to the transition of electrons is facilitated by these surface defects, called active sites, which affects the photochemical and optoelectronic

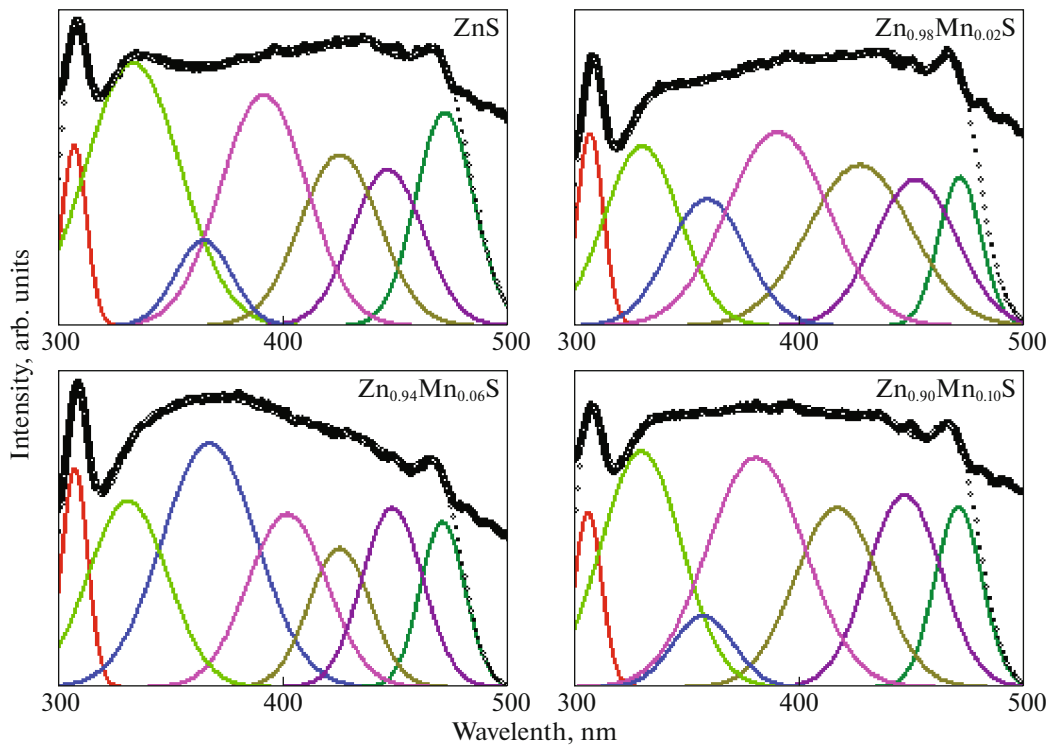


Fig. 6. Deconvoluted PLE plots of the $Zn_{1-x}Mn_xS$ ($x = 0, 0.02, 0.06, 0.10$) QDs.

properties of the QD samples. Out of the active or luminescent site creating defects, namely, the Frenkel and Schottky defects, only one is dominant in a specific substance, because of the relative size of the cation and anion; Schottky defects are usually predominant in ZnS QDs having cubic zinc-blende phase [26]. A perfect lattice deformed by empty sites gives rise to vacancy defects. Energy gap between the valence band (VB) edge and the electron levels originating from zinc or manganese vacancies would be greater than the energy gap between the electron levels originating from the sulphur vacancies and the conduction band (CB) edge, since sulphur atoms are larger in size than zinc or manganese ions. A perfect lattice deformed by extra atoms occupying sites between other atoms gives

rise the interstitial defects. Energy gap between the VB edge and the electron levels originating from sulphur interstitials would be lesser than the energy gap between the electron levels originating from zinc or manganese interstitials and the CB edge, since zinc and manganese ions are smaller in size than sulphur ions [16, 27, 28].

PLE spectra of the $Zn_{1-x}Mn_xS$ ($x = 0, 0.02, 0.06, 0.10$) QDs was deconvoluted and fitted to obtain the list of PLE peaks shown in Table 2.

Excitonic peak is observed at about 307 nm. Strong size confinement in the $Zn_{1-x}Mn_xS$ ($x = 0, 0.02, 0.06, 0.10$) QDs, as confirmed by structural characterizations, leads to a large surface-to-volume ratio, which in turn leads to a very large number of luminescent

Table 2. List of deconvoluted PLE peaks of the $Zn_{1-x}Mn_xS$ ($x = 0, 0.02, 0.06, 0.10$) QDs

EMISSION PEAK	ZnS (pristine), nm	$Zn_{0.98}Mn_{0.02}S$ (nm)	$Zn_{0.94}Mn_{0.06}S$ (nm)	$Zn_{0.90}Mn_{0.10}S$ (nm)
Excitonic	307	307	307	306
Sulphur interstitials	333	330	331	330
Zinc interstitials	364	359	367	357
Zinc vacancies	391	390	401	380
Sulphur vacancies	424	426	424	416
Sulphur vacancies to zinc vacancies	445	451	448	446
Dangling bonds	471	470	470	470

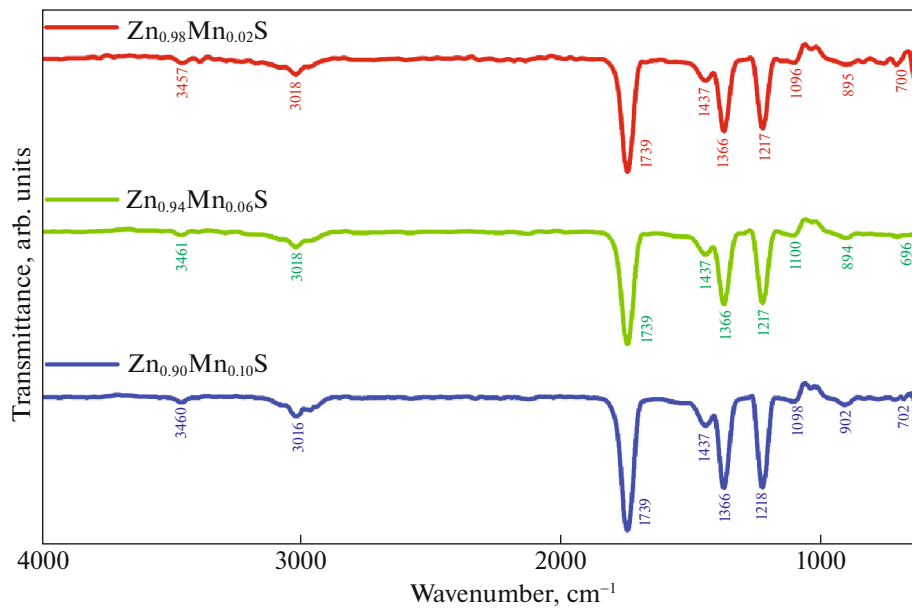


Fig. 7. FTIR spectra of the $Zn_{1-x}Mn_xS$ ($x = 0.02, 0.06, 0.10$) QDs.

surface states, as indicated by the formation of a near continuous band in the PLE spectra from 330 to 440 nm. Transition from the CB to the sulphur interstitial level leads to an observed peak at about 331 nm. Transition from the zinc interstitial level to the VB leads to an observed peak at about 360 nm. Transition from the CB to the zinc vacancy level leads to an observed peak at about 390 nm. Transition from the sulphur vacancy level to the VB leads to an observed peak at about 420 nm. Transition from the donor level of sulphur vacancies to the acceptor level of zinc vacancies leads to an observed peak at about 449 nm. More transitions are facilitated by the weak interaction of various surface states with dangling sulphur bonds, leading to the observed peak at about 470 nm [29–31].

3.6. FTIR Studies

Figure 7 shows the FTIR characteristics of the prepared QDs in the 600–4000 cm^{-1} range. The bands produced from 695 to 706 cm^{-1} are due to the stretching vibrations of Zn–S [32]. The additional asymmetric stretching band can be observed near 900 cm^{-1} ; also, bands between 900–1500 cm^{-1} are due to the oxygen stretching and bending frequency [33].

The absorption bands near to 1740 and 3018 cm^{-1} are due to C=O and C–H stretching vibrations, respectively. It has been reported by several authors reported that around 3400 cm^{-1} absorption band exist due to the OH^- ions stretching [34, 35]. Certain degree of humidity always presents in air atmosphere; from which OH^- ions get trapped inside the crystal lattice.

CONCLUSIONS

Zinc-blende structure type cubic Mn-doped ZnS QDs with the generic formula $Zn_{1-x}Mn_xS$ ($x = 0, 0.02, 0.06, 0.10$) have been successfully synthesized using simple co-precipitation method, which was confirmed by P-XRD patterns. The crystallite size calculated using well known Scherrer formula was found to lie in the range of 1.90–2.35 nm, which was also confirmed by HRTEM analysis. Also, SAED pattern of HRTEM confirms the presence of three diffraction planes discussed in the P-XRD pattern. A pronounced blue shift (~ 33 nm) due to the quantum confinement was observed in the absorption edges Mn-doped ZnS QDs as compared to its bulk counterparts, which confirms quantum dots formation. The photo-luminescence spectra shows the existence of surface defects occurred due to large surface to volume ratio.

FUNDING

One of the authors, Ravi Kant Choubey is thankful to the Council of Science and Technology, Lucknow, Uttar Pradesh, India for the financial support (Vide no. CST/4051).

CONFLICT OF INTEREST

The authors declare that they have no conflict of interest.

REFERENCES

1. A. P. Alvim, Science (Washington, DC, U. S.) **271**, 933 (1996).
2. L. E. Brus, Phys. Chem. Solids **59**, 459 (1998).

3. S. Kumar, H. C. Jeon, T. W. Kang, R. Singh, J. K. Sharma, and R. K. Choubey, *J. Mater. Sci.: Mater. Electron.* **26**, 3939 (2015).
4. B. Xie, R. Hu, and X. Luo, *J. Electron. Packag.* **138**, 020803 (2016).
5. J. K. Oh, *J. Mater. Chem.* **20**, 8433 (2010).
6. S. D. Sartale, B. R. Sankapal, M. Lux-Steiner, and A. Ennaoui, *Thin Solid Films* **480–481**, 168 (2005).
7. D. A. Johnston, M. H. Carletto, K. T. R. Reddy, I. Forbes, and R. W. Miles, *Thin Solid Films* **403–404**, 102 (2002).
8. Y. Changhui, F. Xiaosheng, L. Guanghai, and Z. Lide, *Appl. Phys. Lett.* **85**, 3035 (2004).
9. J. Selvaraj, A. Mahesh, V. Baskaralingam, A. Dhayalan, and T. Paramasivam, *New J. Chem.* **3**, 288 (2019). <https://doi.org/10.1039/c9nj02222h>
10. J. Ouyang, M. Vincent, D. Kingston, P. Descours, T. Boivineau, M. B. Zaman, X. Wu, and K. Yu, *J. Phys. Chem. C* **113**, 5193 (2009).
11. V. Wood, J. E. Halpert, M. J. Panzer, M. G. Bawendi, and V. Bulovic, *Nano Lett.* **9**, 2367 (2009).
12. Y.-C. Fang, S.-Y. Chu, H.-C. Chen, P.-C. Kao, I.-G. Chen, and C.-S. Hwang, *J. Electrochem. Soc.* **156**, K55 (2009).
13. T. P. Surkova, V. R. Galakhov, and E. Z. Kurmaev, *Low Temp. Phys.* **35**, 79 (2009).
14. W. H. Zhao, Z. Q. Wei, L. Zhang, X. J. Wu, X. Wang, and J. L. Jiang, *J. Alloys Compd.* **698**, 754 (2017).
15. G. S. Harish and P. Sreedhara Reddy, *AIP Conf. Proc.* **1536**, 121 (2013).
16. S. Gupta, R. K. Choubey, L. K. Sharma, M. P. Ghosh, M. Kar, and S. Mukherjee, *Semicond. Sci. Technol.* **34**, 105006 (2019).
17. J. Liu, J. Ma, Y. Liu, Z. Song, Y. Sun, J. Fang, and Z. Liu, *J. Alloys Compd.* **486**, L40 (2009).
18. A. L. Patterson, *Phys. Rev.* **56**, 978 (1939).
19. E. O. Kane, *Phys. Rev. B* **18**, 6849 (1978).
20. J. Nanda, S. Sapra, and D. D. Sarma, *Chem. Mater.* **12**, 1018 (2000).
21. J. Tauc and A. Menth, *J. Non-Cryst. Solids*, Nos. 8–10, 569 (1972).
22. L. E. Brus, *J. Chem. Phys.* **79**, 5566 (1983).
23. H. Shen, C. Zhou, S. S. Xu, C. Yu, H. Wang, X. Chen, and L. S. Li, *J. Mater. Chem.* **21**, 6046 (2011).
24. L. Chen, C. Wang, Q. Li, S. Yang, L. Hou, and S. Chen, *J. Mater. Sci.* **44**, 3413 (2009).
25. Y. Li, Y. Ding, Y. Zhang, and Y. Qian, *J. Phys. Chem. Solids* **60**, 13 (1999).
26. A. A. Zarandi, A. A. S. Alvani, R. Salimi, H. Sameie, S. Moosakhani, D. Poelman, and F. Rosei, *J. Mater. Chem. C* **3**, 3935 (2015).
27. A. K. Shahi, B. K. Pandey, R. K. Swarnkar, and R. Gopal, *Appl. Surf. Sci.* **257**, 9846 (2011).
28. L. K. Sharma and S. Mukherjee, *J. Electron. Mater.* **46**, 1270 (2016).
29. S. Wageh, Z. S. Ling, and X. Xu-Rong, *J. Cryst. Growth* **255**, 332 (2003).
30. R. Shahid, M. Toprak, H. Soliman, and M. Muhammed, *Open Chem.* **10**, 54 (2012).
31. M. Kuppayee, G. K. V. Nachiyar, and V. Ramasamy, *Mater. Sci. Semicond. Process.* **15**, 136 (2012).
32. A. Jain, S. Panwar, T. W. Kang, H. C. Jeon, S. Kumar, and R. K. Choubey, *J. Mater. Sci.: Mater. Electron.* **25**, 1716 (2014).
33. B. S. Remadevi, R. Raveendran, and A. V. Vaidyan, *Pramana J. Phys.* **68**, 679 (2007).
34. I. Ahemen, O. Meludu, and E. Odoh, *Braz. J. Appl. Sci. Technol.* **3**, 1228 (2013).